Molecular mechanism of RUVBL1/2-TTT complex assembly by GNB1L

Authors: Junfei Guo[1†], Guangxian Wang[1†], Weiwang Tang[1], Zexuan Zheng[1], Zihan Zhang[1], Junxiang Cui[1], Gang Cai[1,2*], Xuejuan Wang[1*]

Affiliations:

[1] Department of Radiation Oncology, the First Affiliated Hospital of USTC, MOE Key Laboratory for Cellular Dynamics, Center for Advanced Interdisciplinary Science and Biomedicine of IHM, Division of Life Sciences and Medicine, University of Science and Technology of China, Hefei, Anhui, China 230027.

[2] Key Laboratory of Anhui Province for Emerging and Reemerging Infectious Diseases, Hefei, Anhui, China.

† These authors contributed equally to this work.

* Correspondence: Xuejuan Wang (xuejuan@ustc.edu.cn) and Gang Cai (gcai@ustc.edu.cn)

This PDF file includes:

Materials and Methods
Extended Data Fig. 1 to 18
Extended Data Table 1
References

Materials and Methods

Antibodies

HRP-conjuagated FLAG-tag mouse monoclonal antibody was used at 1:2000 dilution (ABclonal, AE095), HRP-conjuagated Myc-tag mouse monoclonal antibody was used at 1:1000 dilution (Abmart, M20019). Anti-Strep II-tag mouse monoclonal antibody was used at 1:2000 dilution (ABclonal, AE066). Anti-TELO2 rabbit monoclonal antibody (ABclonal, A17064). Anti-GNB1L rabbit polyclonal antibody (ABclonal, A7810).The secondary antibodies HRP conjugated goat anti-mouse IgG was used at 1:5000 dilution (Abmart, M21001), HRP Conjugated goat anti-rabbit IgG was used at 1:5000 dilution (Abmart, M21002).

Cloning and mutagenesis

Human RUVBL1, RUVBL2, GNB1L, TELO2, TTI1, and TTI2 cDNAs were amplified by PCR and subcloned into the MultiBac 4V1R vector by homologous recombination, each with distinct affinity tags. One construct encoded RUVBL1 and RUVBL2, with RUVBL1 fused to an N-terminal Strep-tag II. A second construct (provided by Dr. Yue Qin) encoded GNB1L, TELO2, TTI1, and TTI2, with GNB1L carrying an N-terminal FLAG tag. TEV protease was co-expressed in both vectors, and a TEV cleavage site was introduced between each protein.

RUVBL1/RUVBL2 mutants (RUVBL1 H18A/H20A; RUVBL2 H25A/H27A) and a truncation mutant (RUVBL1 Δswitch loop, residues 253–266) were generated by two-step PCR using the wild-type RUVBL1/2 vector as template for ATPase activity and pull-down assays. In parallel, a TELO2 truncation (residues 563–571) was introduced into the GNB1L-TELO2-TTI1-TTI2 construct for pull-down assays. Additional constructs included a 4V1R vector encoding TELO2, TTI1, and TTI2, with TELO2 fused to an N-terminal FLAG tag and TTI2 fused to a C-terminal Myc tag. On this basis, truncations of the N-terminus (residues 1–100) and C-terminus (residues 302–508) of TTI2 were generated. At same the time, 4V1R vectors of GNB1L without tags and with N-terminal Flag tag were constructed for Pull-down assays and ATPase activity assays. All constructs were verified by DNA sequencing.

Protein expression and purification

The human TTT-RUVBL1/2-GNB1L complex was recombinantly expressed using the MultiBac baculovirus system. Full-length open reading frames (ORFs) of all subunits were cloned into two MultiBac 4V1R transfer vectors (RUVBL1/2;GNB1L-TELO2-TTI1-TTI2). Each vector was transformed into *E. coli* DH10Bac cells (TOLOBIO) to generate recombinant bacmid DNA. Bacmid DNA was subsequently isolated and transfected into *Sf9* insect cells (6-well plates) using FuGENE® HD transfection reagent (Promega). P0 virus was harvested at 5 days post-transfection and subsequently amplified in Sf9 suspension cultures grown in SF Vir-exp CDM medium (OPM). Infect *Sf9* cells with P0(1:100) for 5 days to produce P1.For large-scale protein production, *Sf9* cells were infected with amplified P1 virus and cultured at 27°C for 48 hours.

Cells were harvested by centrifugation, resuspended in lysis buffer (40 mM HEPES pH 7.4, 50 mM NaCl, 1 mM EDTA, 1 mM TCEP, 10% (v/v) glycerol, 0.3% (m/v) CHAPS), and lysed by homogenization.

The crude lysate was clarified by ultracentrifugation at 40,000 rpm for 40 minutes. The supernatant was incubated with anti-FLAG M2 affinity resin (Sigma) for 2 hours at 4°C. The resin was then washed extensively with lysis buffer, and bound proteins were eluted using lysis buffer supplemented with 0.2 mg/mL 3×FLAG peptide (APExBIO). The eluate was concentrated using a 10 kDa molecular weight cut-off (MWCO) Amicon Ultra centrifugal filter (Merck Millipore). The complex was further purified by size-exclusion chromatography (SEC) on a Superose™ 6 Increase 10/300 column (Cytiva) equilibrated with SEC buffer (40 mM HEPES pH 7.4, 50 mM NaCl, 1 mM EDTA, 1 mM TCEP, 2% (v/v) glycerol, 0.1% (m/v) CHAPS). Peak fractions corresponding to the intact TTT-RUVBL1/2-GNB1L complex were pooled, concentrated, and flash-frozen in liquid nitrogen for storage. Protein concentration was determined by Bradford assay.

Wild-type RUVBL1/RUVBL2, RUVBL1/RUVBL2 quadruple histidine mutant (RUVBL1 H18A/H20A; RUVBL2 H25A/H27A) and RUVBL1 truncation mutant (Δswitch loop, residues 253–266) were expressed in *Sf9* cells and purified using Streptavidin Beads 6FF (Smart-lifesciences) in lysis buffer containing 40 mM HEPES pH 7.4, 50 mM NaCl, 1 mM TCEP, 10% (v/v) glycerol, and 0.3% (m/v) CHAPS. RUVBL1/RUVBL2-TELO2-TTI1-TTI2 (with TELO2 fused to an N-terminal FLAG tag), GNB1L with an N-terminal FLAG tag and the TELO2–TTI1–TTI2 complex (with TELO2 fused to an N-terminal FLAG tag) were expressed in *Sf9* cells, proteins were purified using Anti-DYKDDDDK Affinity Beads (Smart-lifesciences) in the same lysis buffer.

All protein samples were further purified by size-exclusion chromatography (SEC) on a Superose™ 6 Increase 10/300 column (Cytiva).

ATPase activity assay

ATPase activity of RUVBL1/2 was measured using the Kinase-Lumi™ kit (Beyotime). Assays were performed in buffer containing 40 mM HEPES pH 7.4, 50 mM NaCl, 1 mM TCEP, 10% (v/v) glycerol, and 0.3% (m/v) CHAPS. All reactions were carried out in triplicate, and the remainder of the protocol was performed according to the manufacturer's instructions (Beyotime). For mutant assay, 50 nM RUVBL1/2 (wild-type, or mutant) was incubated with or without 150 nM TTT complexes and with or without 50 nM GNB1L in lysis buffer (composition as above) at 4 °C for 1 h (each component is indicated in the figure). ATP and $MgCl_2$ were subsequently added to final concentrations of 2 uM and 5 mM, respectively. And reactions were carried out at 37 °C for 1 h. Kinase activity detection reagent was subsequently added, and the mixture was incubated at room temperature for 10 min. Negative controls included reactions containing ATP alone (2 μM) and/or proteins alone under identical conditions. Luminescence signals were recorded across all wavelengths using a SpectraMax iD5 plate reader (Molecular Devices).

Pull-down assay

Pull-down experiments were performed in *Sf9* cells cotransfected with plasmids as indicated in the figures. Each plasmid was transformed into *E. coli* DH10Bac cells(TOLOBIO) to generate recombinant bacmid DNA. Bacmid DNA was subsequently isolated and transfected into *Sf9* insect cells (6-well plates) using FuGENE® HD transfection reagent (Promega). P0 virus was harvested at 5 days post-transfection and subsequently amplified in *Sf9* suspension cultures grown in SF Vir-exp CDM medium

(OPM). Infect *Sf9* cells with P0(1:100) for 5 days to produce P1. *Sf9* cells were infected with amplified P1 virus and cultured at 27°C for 48 hours. Cells were harvested 48 h post-transfection and lysed in buffer supplemented with protease inhibitors. After centrifugation, the supernatant was incubated with 20 µl Anti-DYKDDDDK Affinity Beads (Smart-lifesciences) at 4 °C for 1 h. Beads were washed three times with lysis buffer, and bound proteins were eluted with lysis buffer containing 3× FLAG peptide. Eluates were analyzed by western blotting. All experiments were independently repeated at least three times.

Mass photometry

To assess the stoichiometry and mass distribution of the TTT-RUVBL1/2 complex upon addition of GNB1L *in vitro*, standard landing assays were performed at 25 °C using a TwoMP instrument (Refeyn) mounted on an active vibration isolation platform. Glass coverslips with silicone gaskets (Refeyn) were cleaned by sequential sonication in 100% (v/v) isopropanol and ultrapure water, followed by plasma glow discharge. Measurements were conducted on both the intact TTT–RUVBL1/2–GNB1L complex and the co-purified TTT-RUVBL1/2 complex. Samples were stored in PBS and applied immediately prior to the acquisition of 60–120 s image series. Bovine serum albumin (BSA; Beyotime) was measured on the same day as a standard to calibrate particle contrast relative to molecular mass. Image sequences were acquired at 488 nm with 8 ms exposure (128 Hz acquisition) over a 1 × 2.17 µm field of view. Frame and pixel binning factors of 3 and 6 were applied, yielding an effective pixel size of 72 nm. Data acquisition and analysis were performed using Refeyn AcquireMP and DiscoverMP software (v2.5).

Cryo-EM Data Acquisition

Cryo-EM data were collected on a Titan Krios G4 transmission electron microscope (Thermo Fisher Scientific) operated at 300 kV, equipped with a Falcon 4i direct electron detector. Automated data acquisition was performed using EPU software. Movies were recorded at a nominal magnification of 130,000× in super-resolution mode, yielding a calibrated pixel size of 0.971 Å. Each movie comprised 32 frames with a total electron dose of approximately 50 $e^-/Å^2$. A total of 4,578 movie stacks were collected.

Cryo-EM Data Processing

Cryo-EM data processing was primarily performed within CryoSPARC[1]， complementarily integrated with cryoDRGN for heterogeneity analysis.[2] Motion correction and contrast transfer function (CTF) estimation were performed on the raw movies. Initial particle picking was carried out using the Blob Picker algorithm. The extracted particles were downsampled fourfold to a box size of 90 pixels and subjected to ab initio reconstruction to generate three initial models. Subsequent heterogeneous refinement partitioned the dataset into three distinct classes, one of which exhibited well-defined structural features. Multiple rounds of heterogeneous refinement and 2D classification were performed to select high-quality particles based on the presence of clear structural definition. Ultimately, a subset of 162,955 particles enriched with sharp secondary structure features was selected and re-extracted at full scale without downsampling (box size of 360 pixels, 0.971 Å/pixel). These particles were further aligned and subjected to local refinement with C1 symmetry, yielding a consensus reconstruction at an overall resolution of 3.36 Å.

Due to the relatively lower resolution observed for the TTT and GNB1L regions, we performed further focused refinement on these components. To resolve these flexible regions, we tested various soft masks-including those encompassing the RUVBL1/2 hexameric ring, individual TTT copies, and the GNB1L-TELO2 C-terminus-coupled with particle subtraction, Bayesian polishing, and local refinement. This focused strategy successfully improved the local resolution of the RUVBL1/2 ring to 3.17 Å and pushed the resolution of the three TTT copies to within 3-5 Å. Crucially, the density for the GNB1L-TELO2 C-terminal region was sufficiently improved to clearly visualize distinct secondary structure features.

Structural analysis indicated conformational heterogeneity in the nucleotide-binding states across different ATPase subunits. To resolve these states, we first performed focused 3D classification using a soft mask encompassing the RUVBL1/2 hexameric region, which yielded six distinct functional classes. Subsequent local refinement of each class allowed us to unambiguously identify four discrete nucleotide-binding states. To completely eliminate potential model bias, the particles from each of the four states were subjected to independent *ab-initio* 3D reconstruction. To further eliminate the possibility of any remaining mixed conformations, these particles were subsequently sub-classified into 2~3 distinct groups through deep 3D classification. The re-classification results aligned consistently with the four primary nucleotide-binding states, with only one or two minor classes showing negligible variance, thereby validating the convergence and accuracy of our structural assignments.

Concurrently, we employed the deep-learning-based algorithm cryoDRGN as a parallel approach to analyze the structural heterogeneity of the same dataset (162,955 particles). Particle poses and CTF parameters were converted to the cryoDRGN format and downsampled to D=90 (Bin4) for neural network training, ultimately generating 20 conformational classes. The particle subsets from these classes were exported back to CryoSPARC for focused refinement and nucleotide-state analysis. These 20 structures were clustered into five major conformational groups, from each of which the representative density map with the sharpest structural features and the highest resolution was selected for presentation. Furthermore, by analyzing the latent space along the first two principal components (PC1 and PC2), we successfully mapped and visualized the continuous conformational changes of the intact TTT-RUVBL1/2-GNB1L complex.

Notably, the nucleotide-binding states independently determined by CryoSPARC focused classification and cryoDRGN exhibited excellent consistency and reproducibility. Local refinement of the selected classes yielded multiple RUVBL1/2-focused maps at resolutions ranging from 3.4 to 4.5 Å. Additionally, global refinement of the full TTT-RUVBL1/2-GNB1L complex on the corresponding particle subsets produced multiple global maps at 3.5 to 4.5 Å resolution.

Model Building

Initial atomic models for all subunits (RUVBL1, RUVBL2, GNB1L, TELO2, TTI1, TTI2) were obtained from the AlphaFold Protein Structure Database[3]. The predicted models of GNB1L, TELO2, TTI1, and TTI2 were rigid-body fitted into the cryo-EM density of the global TTT-RUVBL1/2-GNB1L map using

UCSF Chimera[4], followed by manual adjustment in Coot. RUVBL1 and RUVBL2 models were divided into three domains (residues 1-120, 121-230, and 231-456/463 for RUVBL1 and RUVBL2) for independent rigid-body fitting and subsequent manual rebuilding in Coot[5].

For the TTT subcomplex, we first rigidly fitted the AlphaFold3-predicted overall TTT structure into the high-resolution focused map using UCSF Chimera. Manual model adjustment was subsequently performed in COOT, guided primarily by the clear densities of bulky residues such as phenylalanine, tyrosine, tryptophan, lysine, and arginine, which facilitated sequence assignment. In addition, the length of HEAT repeat segments was consistent with the corresponding α-helical densities in the map, allowing us to trace the orientation of the HEAT repeats with confidence. Finally, the model was refined using COOT's all-atom refinement function, yielding the finalized TTT structure.

For the complete TTT-RUVBL1/2-GNB1L complex model, the refined TTT model was duplicated and rotated to generate three symmetry-related copies, which were then fitted into the corresponding densities in the map. These TTT models were combined with the RUVBL1/2 structure to assemble the full complex. Subsequent manual adjustment and refinement in COOT yielded the finalized TTT-RUVBL1/2-GNB1L model.

Based on the six distinct global maps obtained from 3D classification of the RUVBL1/2 ring, we used the TTT-RUVBL1/2-GNB1L model as a reference and performed independent refinements in COOT for each class. This procedure yielded six complete models of the TTT-RUVBL1/2-GNB1L complex, each exhibiting clear conformational differences. All models were subjected to real-space refinement in PHENIX[6] with three macro-cycles of global minimization, local grid search, and B-factor optimization. To maintain proper geometry, restraints for Ramachandran angles, Cβ deviations, secondary structure (generated by CaBLAM[7] in PHENIX), and non-crystallographic symmetry (where applicable) were applied throughout refinement. The relative weight between the experimental map and the geometric restraints was automatically optimized by PHENIX to prevent overfitting. Model validation was performed using MolProbity as implemented in PHENIX. Refinement and model statistics are given in Extended Data Table 1.

Structure Analysis and Visualization

All molecular graphics and structural analyses were performed using UCSF Chimera and ChimeraX[8].

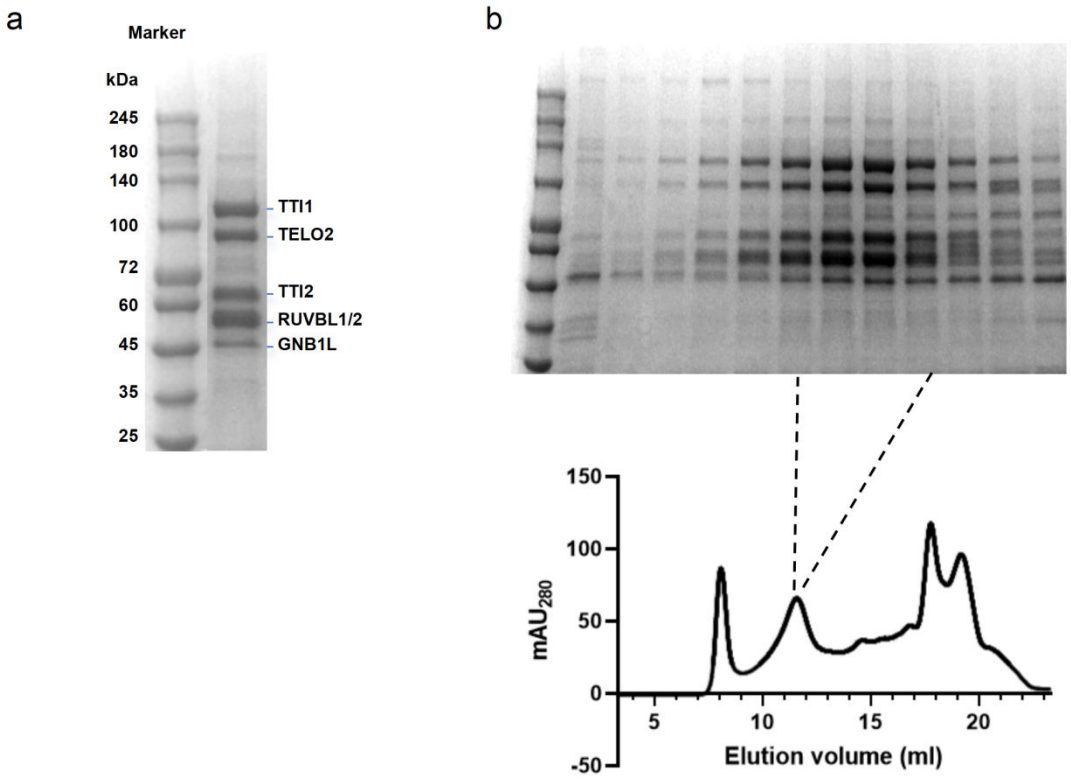

Extended Data Fig. 1 | Purification of the human TTI1-TTI2-TELO2-RUVBL1/2-GNB1L complex. a, SDS-PAGE analysis of the affinity purified TTT-RUVBL1/2-GNB1L complex. **b,** Size-exclusion chromatography of the TTT-RUVBL1/2-GNB1L complex using a Superose 6 Increase column (10/300 GL, Cytiva).

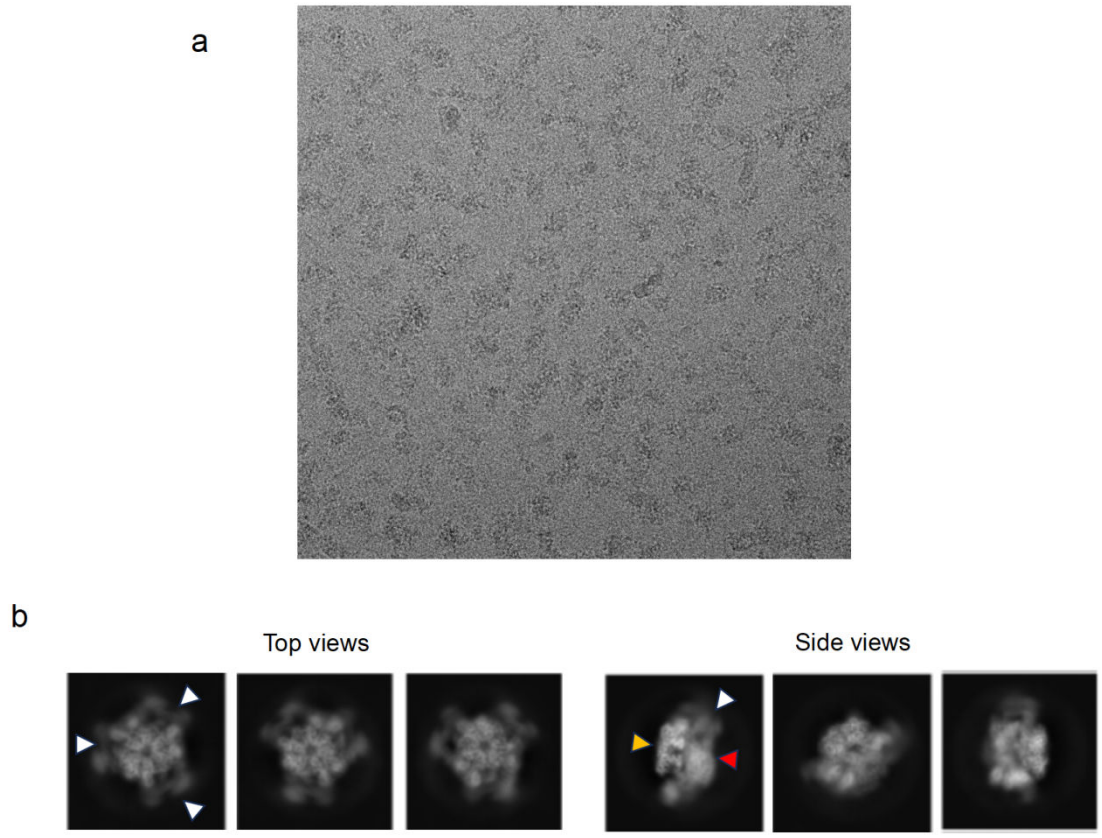

Extended Data Fig.2 | cryo-EM characterization of the human TTT-RUVBL1/2-GNB1L. **a,** Representative cryo-electron micrograph of purified TTT-RUVBL1/2-GNB1L particles embedded in vitreous ice. **b,** Representative 2D class averages of the complex showing top views and side views. Arrowheads indicate key structural features: yellow, the RUVBL1/2 ring; white, the TTT module; Red, GNB1L density located at the bottom of the RUVBL1/2 ring.

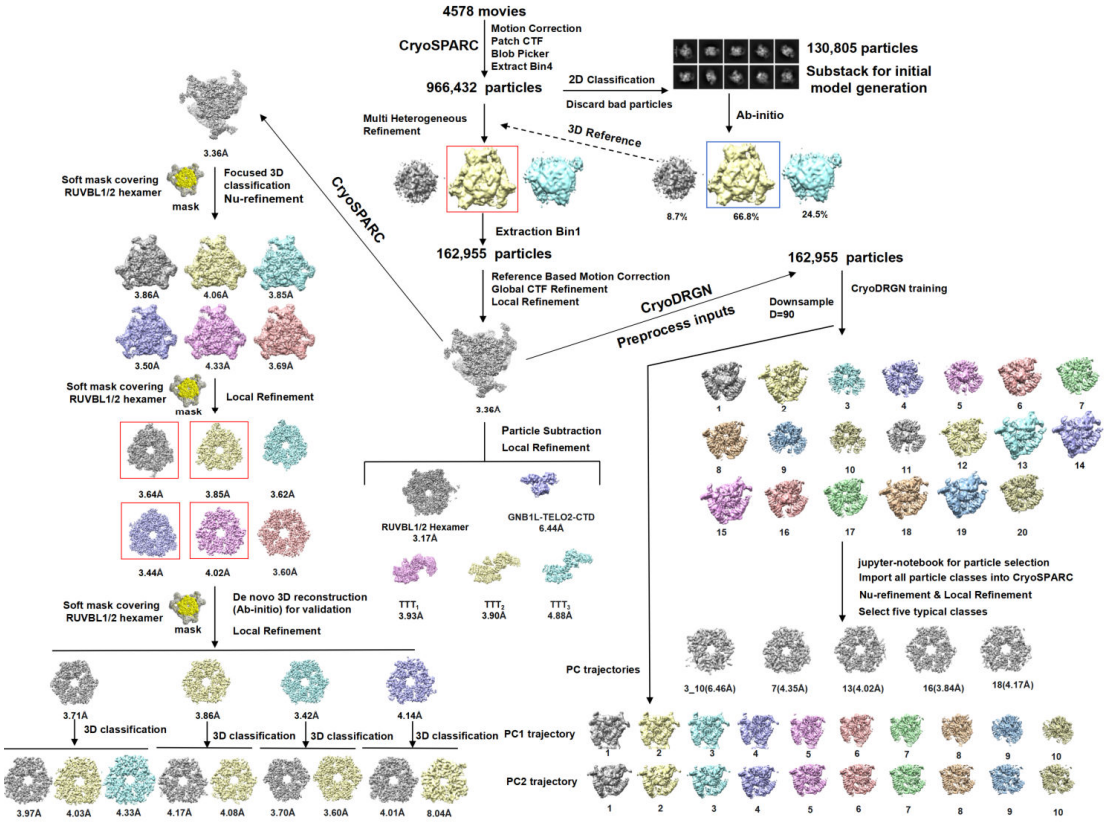

Extended Data Fig.3 | Cryo-EM data processing of human TTT-RUVBL1/2-GNB1L. The schematic diagram illustrates the detailed reconstruction procedures.

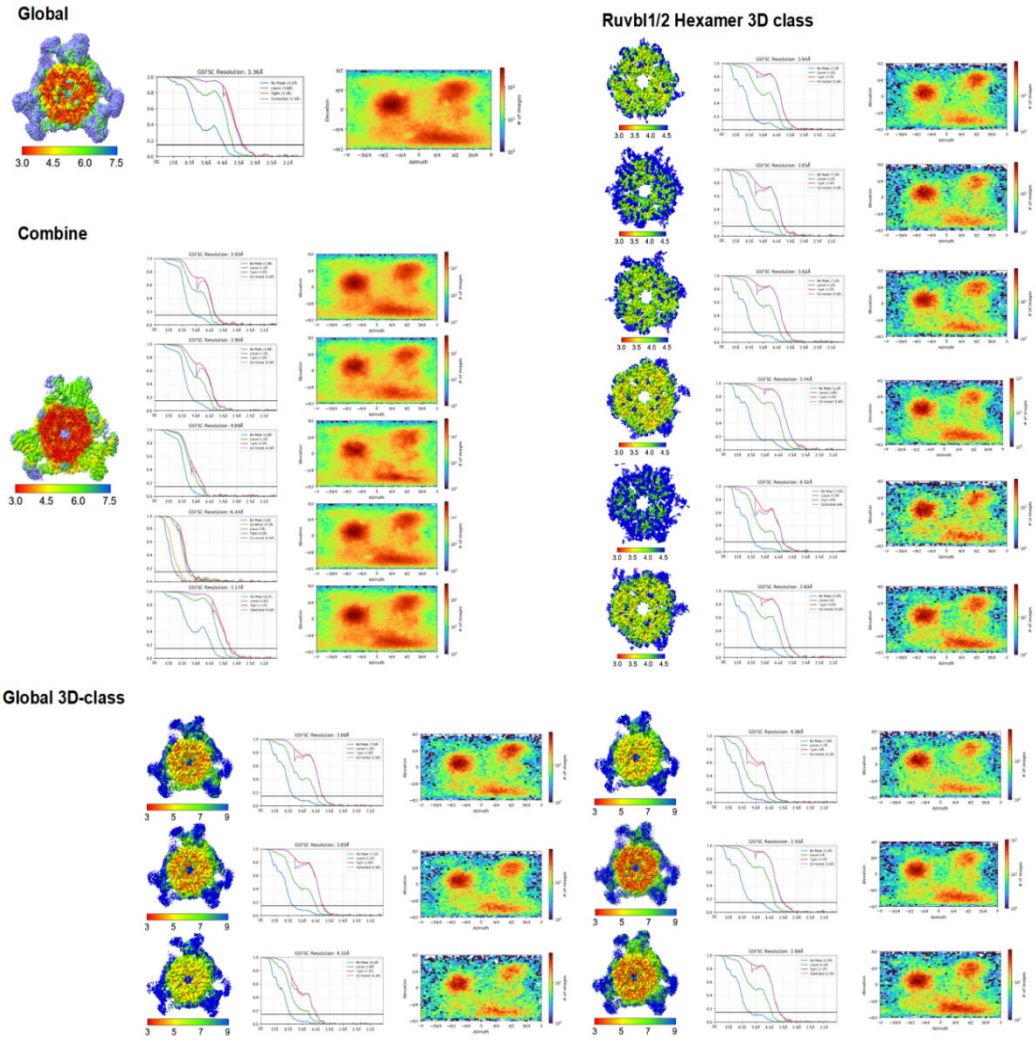

Extended Data Fig. 4 | Cryo-EM map quality metrics for TTT-RUVBL1/2-GNB1L. For the global reconstruction, combined map, and individual 3D classes (including RUVBL1/2 hexamer classes), the local resolution maps (left), gold-standard FSC curves (middle), and angular distributions of particles used for the final reconstructions (right) are shown.

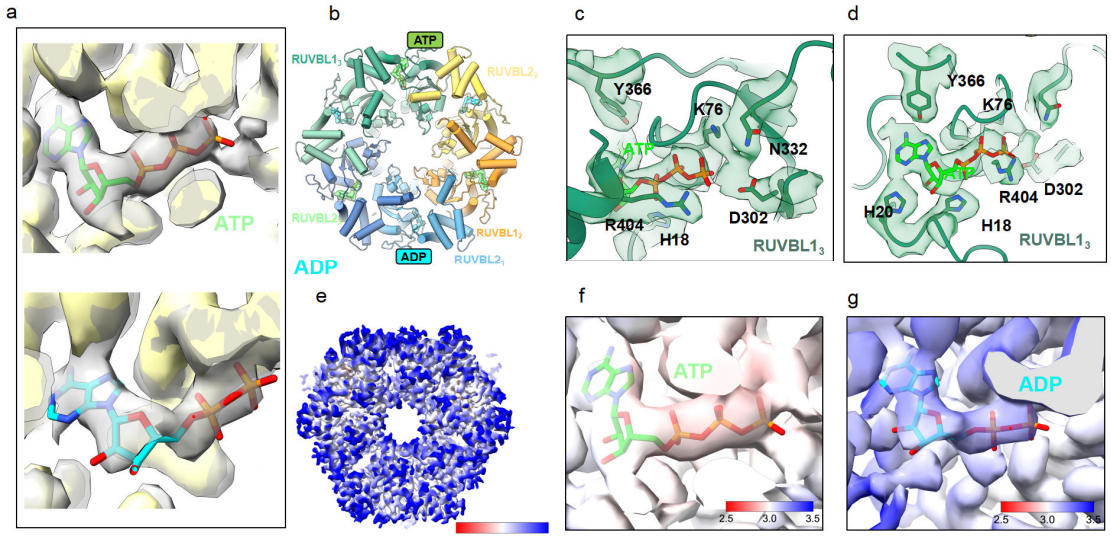

Extended Data Fig. 5 | Detailed views of the nucleotide-binding pockets in RUVBL1 and RUVBL2. a. Validation of nucleotide assignment to rule out model bias or processing artifacts. A nucleotide-free map was used as the initial reference (shown in yellow) for 3D reconstruction/refinement. The resulting reconstructed map (grey) faithfully recovered clear density signals for both ATP (top) and ADP (bottom), confirming the reliability and objectivity of the nucleotide assignments.**b,** Nucleotide occupancy in the RUVBL1/2 hexamer. Without exogenous nucleotides, the 3.36 Å map reveals ATP bound to the three RUVBL1 subunits and ADP bound to the three RUVBL2 subunits.**c,d** Two views of the model-map fitting of the ATP phosphates in the RUVBL1 nucleotide-binding pocket.**e,** Local resolution map of the RUVBL1/2 hexamer, colored according to local resolution estimation (ranging from 2.5 Å to 3.5 Å, as indicated by the color bar).**f,** Zoomed-in view of the ATP-binding pocket embedded in the local resolution cryo-EM map. The bound ATP molecule fits remarkably well into the corresponding density, indicating that the binding pocket resides within a high-resolution region (~2.5-3.0 Å). **g**, Zoomed-in view of the ADP-binding pocket embedded in the local resolution cryo-EM map. The bound ADP molecule fits remarkably well into the corresponding density. Compared with the ATP-binding pocket, this site exhibits higher flexibility, with a local resolution ranging from 3.0 Å to 3.5 Å.

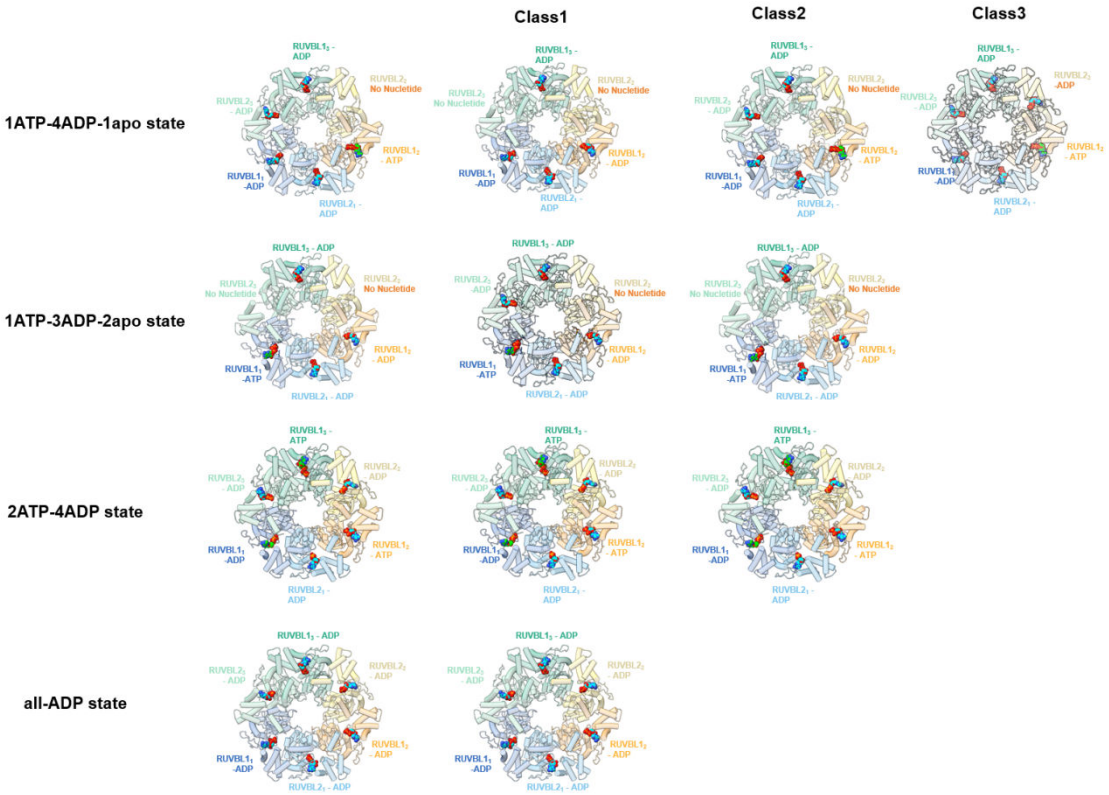

Extended Data Fig. 6 | Conformational heterogeneity and sub-classification of the RUVBL1/2 hexameric states. Sub-classification of the four major nucleotide-bound states of the RUVBL1/2 complex. For each major state, the corresponding particle subsets derived from CryoSPARC processing were subjected to independent *ab-initio* reconstruction followed by further 3D classification, yielding 2~3 sub-classes. Notably, the newly resolved sub-classes show high conformational similarity to their respective original states, validating the stability of the classification. The detailed nucleotide state (ATP, ADP, or *apo* state) for each RUVBL1 subunit (represented in darker shades of blue, yellow, and green) and RUVBL2 subunit (represented in lighter shades of blue, yellow, and green) within the hexameric ring is explicitly labeled and color-coded. Bound ATP and ADP molecules resolved in the respective density maps are shown as lime green and cyan spheres, respectively.

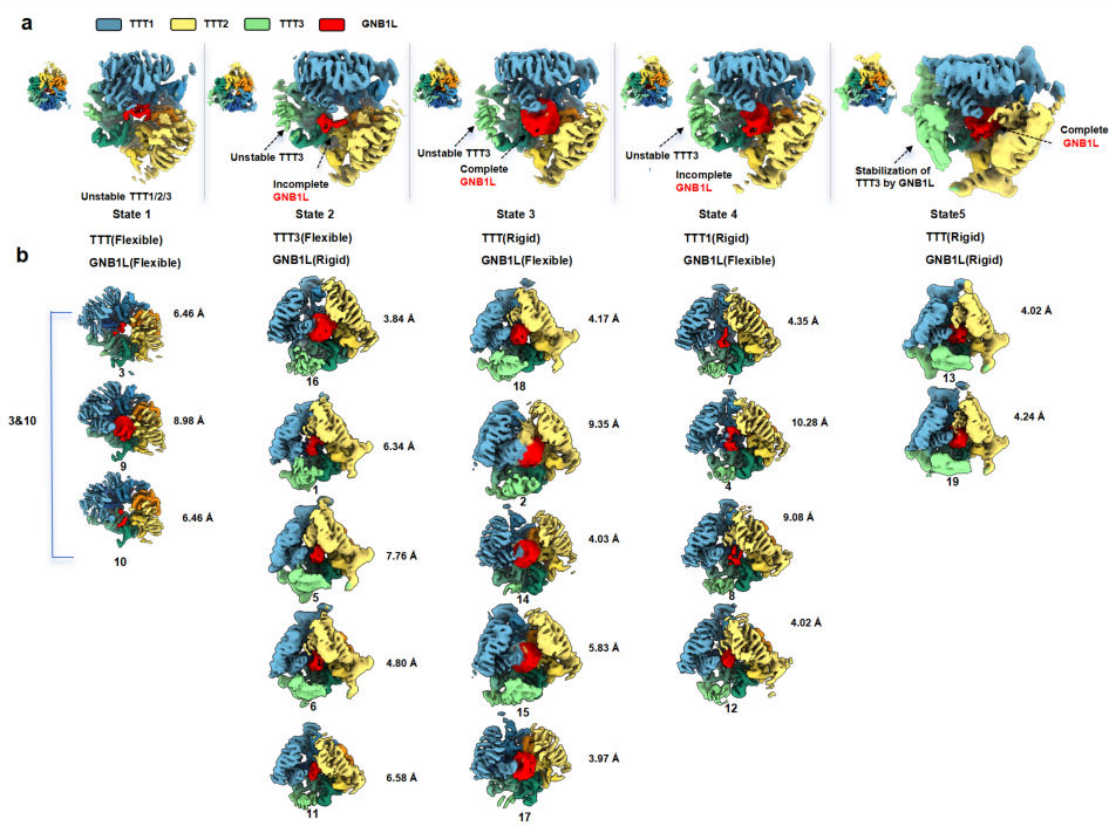

Extended Data Fig. 7 | Cryo-EM heterogenous analysis and classification of human TTT-RUVBL1/2-GNB1L by cryoDRGN. a, Classification of twenty distinct conformational states derived from cryoDRGN neural network analysis. Based on the structural integrity of the TTT region and the GNB1L subunit, these twenty conformations were categorized into five major classes: TTT(Flexible)/GNB1L(Flexible), TTT3(Flexible)/GNB1L(Rigid), TTT(Rigid)/GNB1L(Flexible), TTT1(Rigid)/GNB1L(Flexible), and TTT(Rigid)/GNB1L(Rigid). The smaller inset maps in the upper-left corners are displayed by referencing the RUVBL1/2 hexameric ring to demonstrate consistent density rendering thresholds. **b,** Particles corresponding to these twenty volumes were individually isolated and subjected to focused local refinement in CryoSPARC to optimize the density of the RUVBL1/2 hexameric core. The resulting gold-standard Fourier shell correlation (FSC) resolution for the RUVBL1/2 hexameric ring of each structure is explicitly indicated on its right. Volumes are numbered from 1 to 20 beneath each density map, and the relative orientation of the complexes remains consistent across all classes.

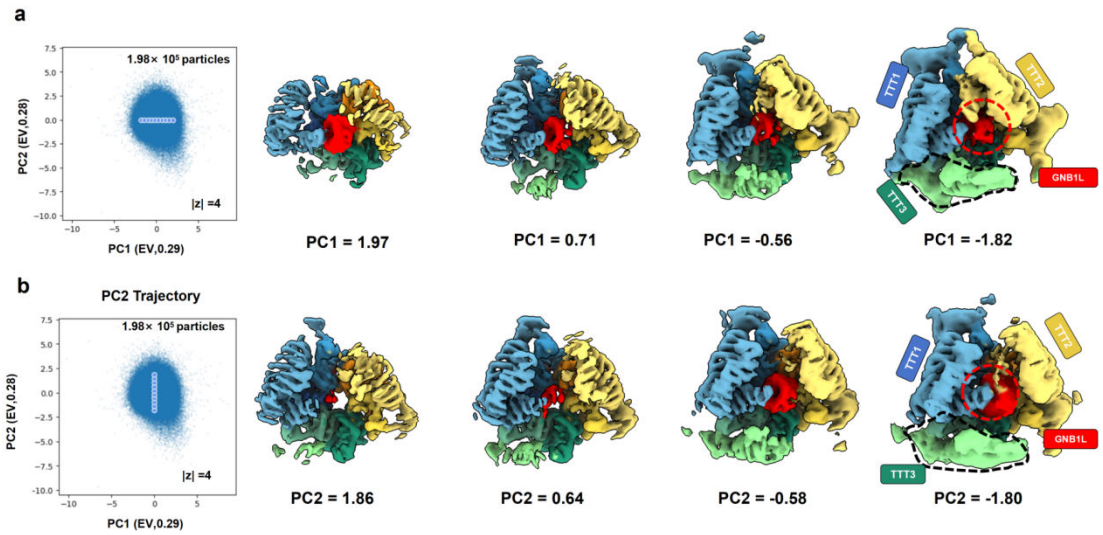

Extended Data Fig. 8 |Characterization of continuous conformational dynamics of the GNB1L and TTT by latent space PCA traversal. a, PCA projection of the latent space encodings obtained after training a 4D latent variable model (|z|=4) in cryoDRGN on the particle dataset (1.98×10^5 particles). Volumes generated by traversing along PC1 at the specific coordinates indicated by the horizontal dots are shown on the right (from PC1= 1.97 to PC1 = -1.82). **b,** PCA projection highlighting the trajectory along PC2 of the same latent space representation. Representative volumes generated by traversing along PC2 at the vertical coordinates are shown on the right (from PC2 = 1.86 to PC2 = -1.80). Labels and dashed outlines indicate the dynamic rearrangement of the TTT subunits (TTT1 in blue, TTT2 in yellow, TTT3 in green) and the coupled movement of GNB1L (red circle).

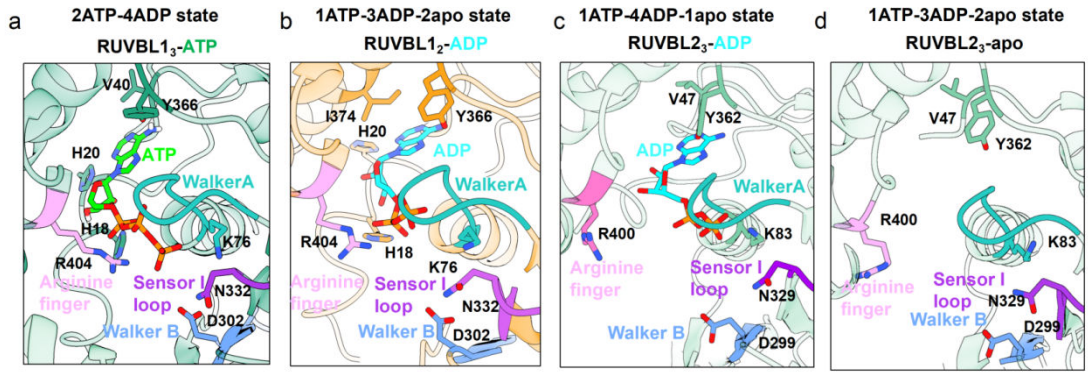

Extended Data Fig. 9 | Nucleotide-binding states of RUVBL1 and RUVBL2. Close-up views of the ATPase pockets in distinct conformational states. **a,** ATP-bound RUVBL1 (RUVBL1$_3$-ATP). **b, c,** ADP-bound RUVBL1 (RUVBL1$_2$-ADP) and RUVBL2 (RUVBL2$_3$-ADP). **d,** Apo RUVBL2 (RUVBL2$_3$-apo). Key nucleotide-sensing elements (Walker A/B, sensor I loop and arginine finger) and interacting residues are indicate

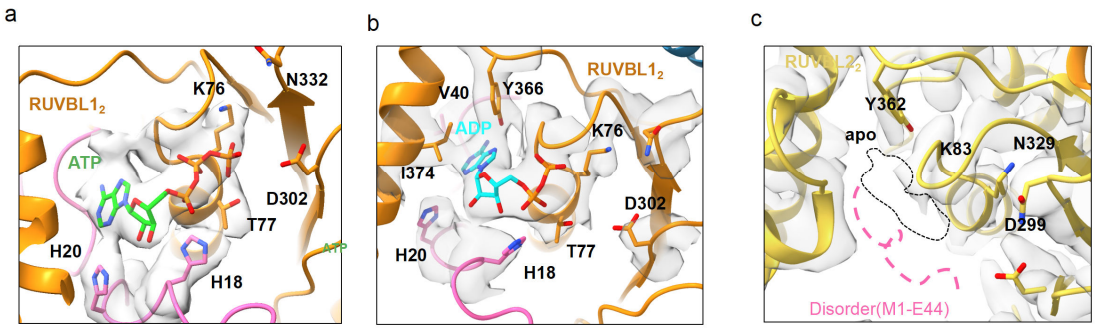

Extended Data Fig. 10 | Coupling between nucleotide state and N-terminal order-disorder transition in RUVBL1/2. a, In the ATP-bound RUVBL1 state, the N terminus (hot pink) is ordered; H18 contacts T77 and H20 engages the adenine base, stabilizing ATP binding. **b,** In the ADP-bound (post-hydrolysis) state, these contacts are lost and the RUVBL1 N terminus becomes destabilized. **c,** In the apo state, nucleotide dissociation coincides with disordering of the RUVBL2 N terminus (M1–E44), with the ATP/ADP-binding site indicated by a black dashed circle.

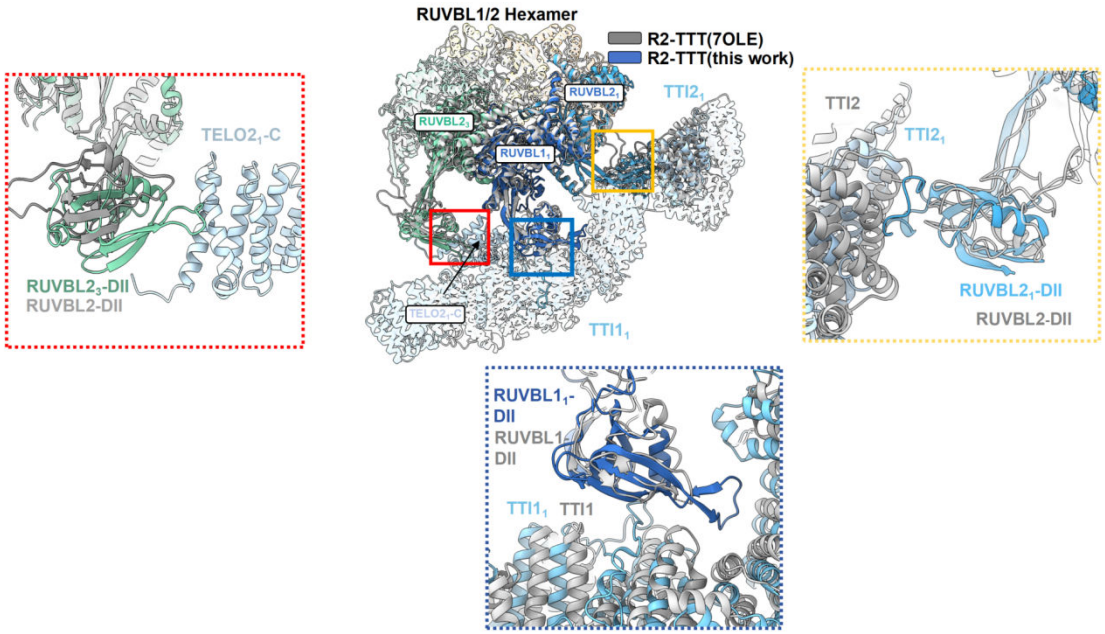

Extended Data Fig. 11 | Comparison of the TTT-RUVBL1/2 interfaces in our TTT-RUVBL1/2-GNB1L structure and the R2-TTT structure (PDB 7OLE). Our TTT-RUVBL1/2-GNB1L model (coloured) is superimposed on the previously reported R2-TTT model (grey)[9]. Regions outside the interfaces are rendered at ~90% transparency. Solid coloured boxes denote three DII-TTT contact sites, with dashed boxes indicating the corresponding magnified views.

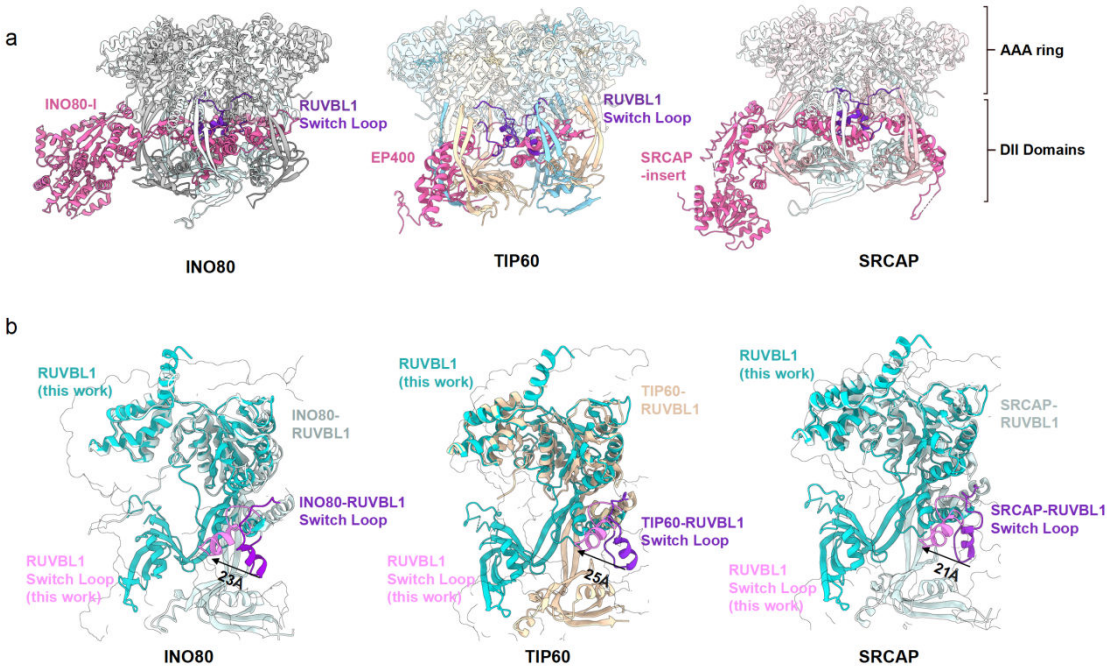

Extended Data Fig. 12 | Comparison of RUVBL1 Switch Loop conformations in the TTT-RUVBL1/2-GNB1L complex and chromatin remodeling complexes. a, RUVBL1-mediated interfaces in the INO80[10], TIP60[11] and SRCAP[12] complexes, highlighting the RUVBL1 Switch Loop and DII domain and the contacting elements (INO80-I, EP400 and the SRCAP insert); remaining regions are shown at ~90% transparency. **b,** Superposition of RUVBL1 from this study with RUVBL1 in INO80, TIP60 and SRCAP, revealing Switch Loop conformational differences and interface shifts (arrows indicate displacements).

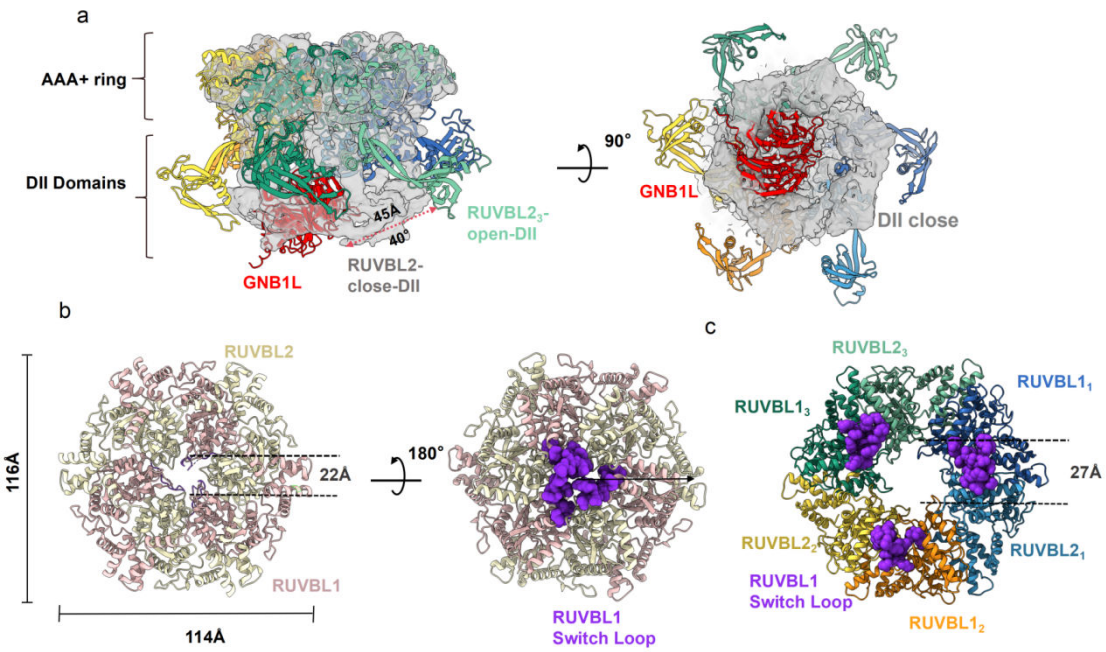

Extended Data Fig. 13 | Comparison of RUVBL1/2-GNB1L and CB-6644-bound RUVBL1/2 structures. **a,** Superposition of the GNB1L-bound RUVBL1/2 atomic model (this study, shown in cartoon) onto the cryo-EM density map of the CB-6644-bound RUVBL1/2 hexamer[13] (EMD-19815; represented as a transparent surface) from two orthogonal views. While the AAA+ rings exhibit minimal structural divergence, a pronounced conformational rearrangement is observed in the DII domains. The top view highlights that the DII domains in the CB-6644-bound state adopt a "closed" conformation that sterically clashes with the GNB1L-binding site, whereas they transition to an "open" state in our complex. **b,** The restricted central pore of the CB-6644-bound RUVBL1/2 hexamer (PDB 9EMA), measuring merely 22 Å in diameter. The RUVBL1 switch loops (colored in purple) cluster inwardly, effectively plugging the central channel. **c,** Expansion of the central pore to 27 Å in our RUVBL1/2-GNB1L complex. The RUVBL1 Switch Loops swing outward into an open conformation, widening and releasing the central pore.

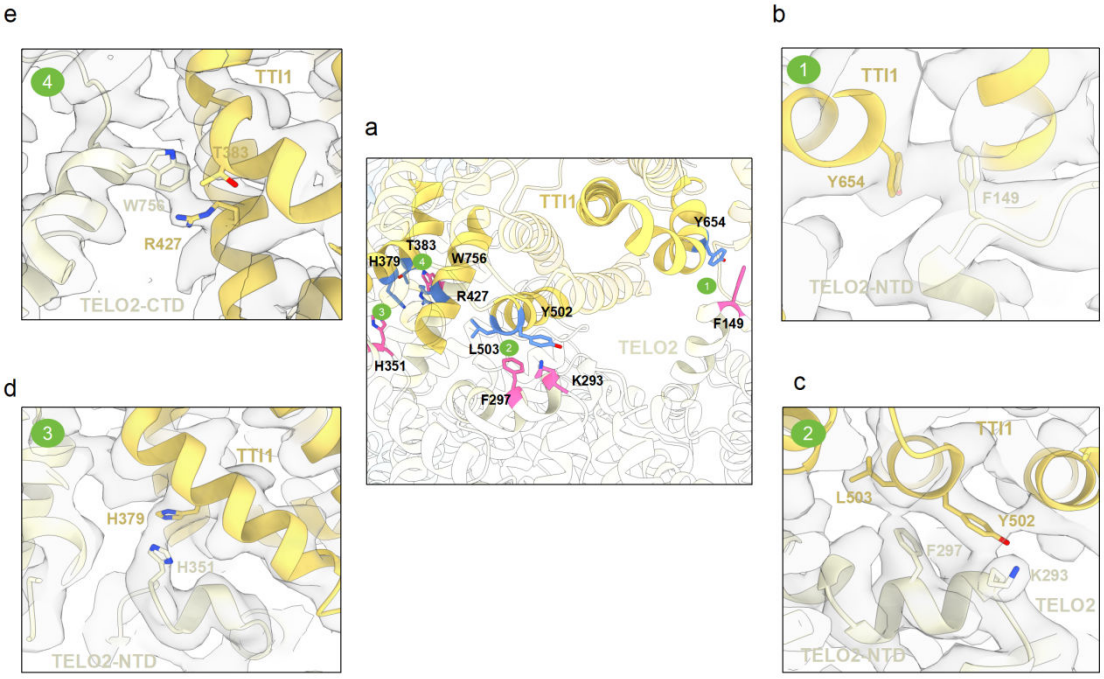

Extended Data Fig. 14 | Detailed interactions between the TTI1 and TELO2 subunits. **a,** Overview highlighting four major contact sites: sites 1-3 map to the TTI1-TELO2 NTD interface, whereas site 4 involves the TTI1-TELO2 CTD. **b-e,** Close-up views of each site shown as model-map overlays.

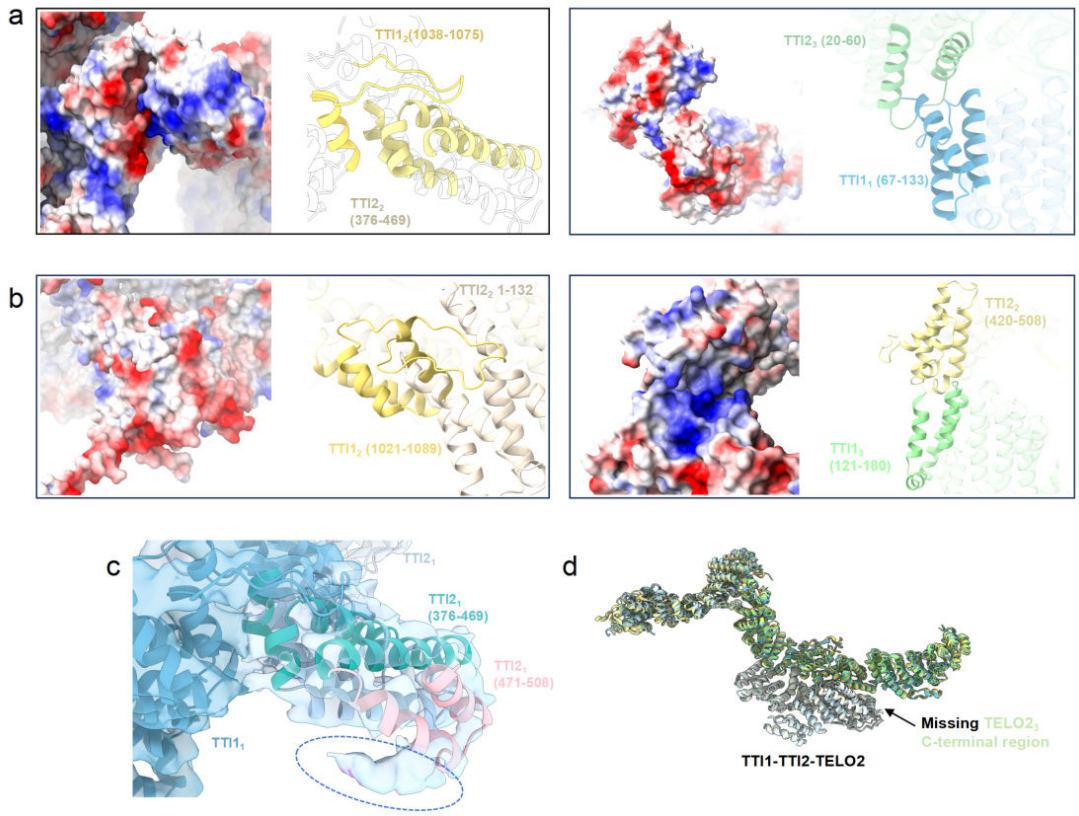

Extended Data Fig. 15 | Electrostatic TTI1-TTI2 interface and TELO2 CTD disorder in TTT_3. a, Surface electrostatic potentials at the $TTI2_2$-$TTI1_2$ and $TTI2_2$-$TTI1_1$ interfaces show strong charge complementarity. **b,** Structural comparison with the previously reported TTT model (PDB: 7OLE). Compared with our model, the orientation of TTI2 in PDB 7OLE is completely reversed; structural analysis indicates that if built according to their reported orientation, distinct electrostatic repulsion (charge clash) occurs between TTI2 and the flanking TTI1 subunits on both sides, thereby validating the rationality of our model conformation. **c,** Model-in-map fitting at the $TTI2_1$-$TTI1_1$ interface. The density-to-model fit demonstrates that the specific region of $TTI2_1$ contacting $TTI1_1$ spans residues 376-469 (rendered as light sea green), rather than the extreme C-terminal tail (residues 471-508, colored in hot pink).The unassigned density enclosed by the blue dashed oval corresponds to a helical segment of TTI1 (residues 806–821) predicted by AlphaFold to interact with TTI2. **d,** Superposition of the three TTT copies (TTT1, blue; TTT2, yellow; TTT3, green) in the TTT-RUVBL1/2-GNB1L complex reveals the C-terminus domain of TELO2 is in a flexible, disordered state in TTT_3

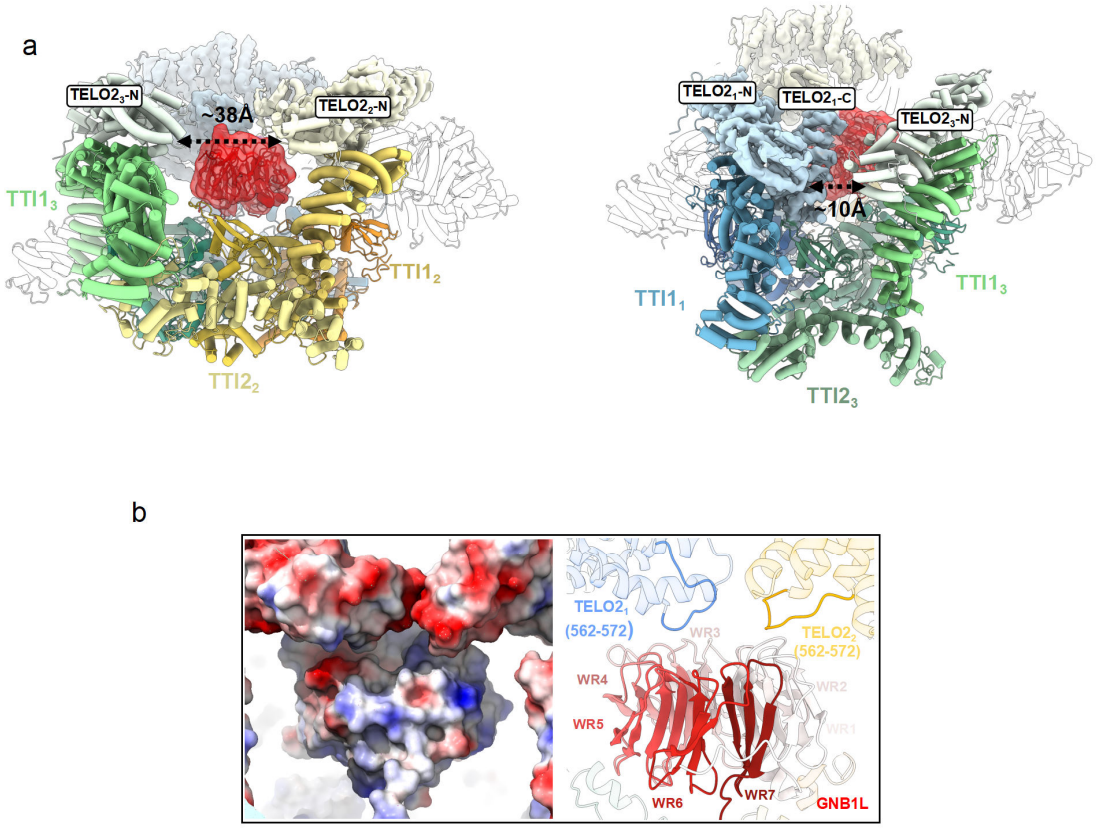

Extended Data Fig. 16 | Structural details of GNB1L-TELO2 interface. a, Surface electrostatics show strong charge complementarity between GNB1L and the TELO2-CTD loop (residues 562-572), indicating electrostatically driven binding. **b,** Side views show that GNB1L binding alters TTT conformation: when the TELO2$_3$ CTD is disordered, TELO2$_3$-N and TELO2$_2$-N are ~38 Å apart, whereas a stable TELO2$_1$ CTD corresponds to a ~10 Å separation between TELO2$_1$-N and TELO2$_3$-N.

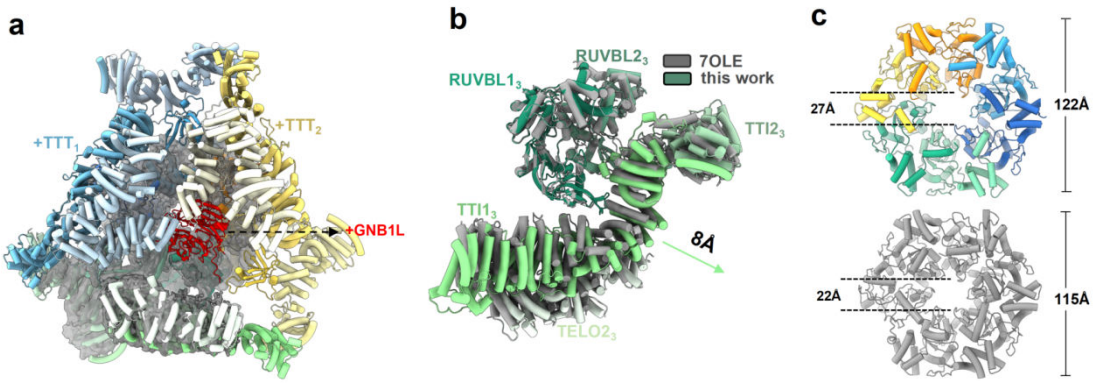

Extended Data Fig. 17 | Structural comparison between the GNB1L-bound and GNB1L-free TTT-RUVBL1/2 complexes. a, Bottom view showing the superposition of the TTT-RUVBL1/2-GNB1Lmodel (this study) onto the cryo-EM map of the RUVBL1/2-TTT complex (EMD-12979)[9]. **b,** Structural alignment of a single structural unit (comprising RUVBL1, RUVBL2, and TTT) from the TTT-RUVBL1/2-GNB1L complex (green) and the RUVBL1/2-TTT complex (PDB: 7OLE, gray), illustrating the relative conformational displacement of TTT. **c,** Comparison of the hexameric ring diameter and central pore aperture of the RUVBL1/2 hexamer between the TTT-RUVBL1/2-GNB1L complex (colored) and the RUVBL1/2-TTT complex (PDB: 7OLE, gray).

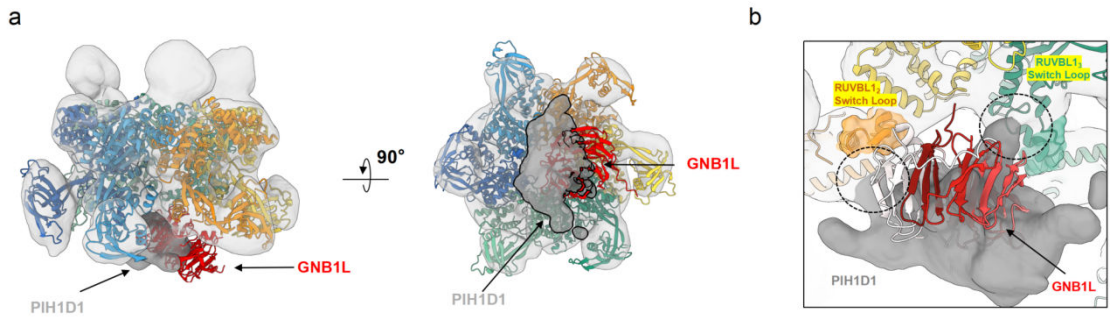

Extended Data Fig. 18 | Structural comparison of the RUVBL1/2-GNB1L with RUVBL1/2-PIH1D1 complex. **a,** Our model was superimposed onto the RUVBL1/2-PIH1D1 density map (EMD-4290); side and bottom views show that GNB1L and PIH1D1 both bind the underside of the RUVBL1/2 ring and occupy an overlapping spatial region. **b,** Close-up comparison indicates that GNB1L and PIH1D1 engage RUVBL1/2 at an essentially equivalent site and with a highly similar binding mode.

Extended Data Table 1. Statistics of 3D reconstruction and model refinement

	Global R2-GNB1L-TTT PDB:21XP (EMD-68074)	Composite map R2-GNB1L-TTT (EMD-68073)	2ATP-4ADP state PDB:21ZU (EMD-68126)	1ATP-4ADP-1apo state PDB:22BL (EMD-68154)	All-ADP state PDB:22AN (EMD-68136)	1ATP-3ADP-2apo state PDB:21XV (EMD-68080)
Date collection and processing						
EM equipment	Titan Krios G4					
Detector	Falcon 4i					
Magnification	130,000					
Voltage(kV)	300					
Electron exposure(e/Å2)	50					
Defocus range (μm)	-1.5 to -2.5					
Pixel size(Å)	0.971					
Frames	32					
Symmetry imposed	C1					
Initial particle images	966,432	966,432	162,578	162,578	162,578	162,578
Final particle images	162,578	162,578	33,673	28,340	20,787	22,870
Map resolution (Å)	3.36		3.5	3.86	4.4	4.06
FSC threshold	0.143		0.143	0.143	0.143	0.143
Model building						
Software	Coot					
Refinement						
Software	Phneix					
Model-map scores						
CC(mask)	0.71		0.67	0.71	0.73	0.75
CC(box)	0.73		0.69	0.75	0.80	0.80
CC (peaks)	0.58		0.52	0.60	0.63	0.64
CC (volume)	0.69		0.66	0.71	0.73	0.74
R.m.s deviations						
Bond length(Å)	0.003		0.002	0.002	0.002	0.002
Bond angles(°)	0.626		0.495	0.476	0.498	0.465
Clashscore	9		7	7	8	8
MolProbity score	2.15		2.57	2.43	2.01	1.97
Ramachandran plot						
Favored (%)	94.39		91.48	91.22	88.95	90.72
Alowed (%)	5.46		8.26	8.58	10.49	8.92
Outlier (%)	0.15		0.26	0.20	0.56	0.36

References

1. Punjani, A., Rubinstein, J.L., Fleet, D.J. & Brubaker, M.A. cryoSPARC: algorithms for rapid unsupervised cryo-EM structure determination. *Nat Methods* **14**, 290-296 (2017).
2. Zhong, E.D., Bepler, T., Berger, B. & Davis, J.H. CryoDRGN: reconstruction of heterogeneous cryo-EM structures using neural networks. *Nat Methods* **18**, 176-185 (2021).
3. Jumper, J. et al. Highly accurate protein structure prediction with AlphaFold. *Nature* **596**, 583-589 (2021).
4. Pettersen, E.F. et al. UCSF Chimera--a visualization system for exploratory research and analysis. *J Comput Chem* **25**, 1605-12 (2004).
5. Emsley, P. & Cowtan, K. Coot: model-building tools for molecular graphics. *Acta Crystallogr D Biol Crystallogr* **60**, 2126-32 (2004).
6. Terwilliger, T.C., Ludtke, S.J., Read, R.J., Adams, P.D. & Afonine, P.V. Improvement of cryo-EM maps by density modification. *Nat Methods* **17**, 923-927 (2020).
7. Prisant, M.G., Williams, C.J., Chen, V.B., Richardson, J.S. & Richardson, D.C. New tools in MolProbity validation: CaBLAM for CryoEM backbone, UnDowser to rethink "waters," and NGL Viewer to recapture online 3D graphics. *Protein Sci* **29**, 315-329 (2020).
8. Goddard, T.D. et al. UCSF ChimeraX: Meeting modern challenges in visualization and analysis. *Protein Sci* **27**, 14-25 (2018).
9. Pal, M. et al. Structure of the TELO2-TTI1-TTI2 complex and its function in TOR recruitment to the R2TP chaperone. *Cell Rep* **36**, 109317 (2021).
10. Ayala, R. et al. Structure and regulation of the human INO80-nucleosome complex. *Nature* **556**, 391-395 (2018).
11. Yang, Z. et al. Structural insights into the human NuA4/TIP60 acetyltransferase and chromatin remodeling complex. *Science* **385**, eadl5816 (2024).
12. Yu, J. et al. Structural insights into histone exchange by human SRCAP complex. *Cell Discov* **10**, 15 (2024).
13. García-Martín, C., López-Perrote, A., Boskovic, J. & Llorca, O. Mechanism of allosteric inhibition of RUVBL1-RUVBL2 ATPase by the small molecule CB-6644. *Cell Reports Physical Science* (2024).